Primary and secondary breakup of molten Ti64 in an EIGA atomizer for metal powder production

Baraa Qaddah, Pierre Chapelle, Jean-Pierre Bellot, Julien Jourdan, Gagan Kewalramani, Agathe Deborde, Raphael Hammes, Nicolas Rimbert

Primary and secondary breakup of molten Ti64 in an EIGA atomizer for metal powder production.

Baraa Qaddah[1], Pierre Chapelle[2,*], Jean Pierre Bellot[2], Julien Jourdan[2], Gagan Kewalramani[3], Agathe Deborde[1], Raphael Hammes[1], Nicolas Rimbert[3]

[1] IRT-M2P, 4 rue Augustin Fresnel, 57070 Metz, France.
[2] Institut Jean Lamour, UMR 7198 CNRS, Université de Lorraine, LabEx DAMAS, BP 50840, 54011 Nancy Cedex, France
[3] LEMTA CNRS, Université de Lorraine, 2 Avenue de la Forêt de Haye, 54518 Vandoeuvre-lès-Nancy, France.

Highlights

- High-speed visualization of liquid metal breakup mechanisms in an EIGA atomizer.
- The effect of atomisation pressure and melting chamber pressure is analysed.
- A log-stable law model is presented to describe the measured mass distribution.
- A too low overpressure in the melting chamber favours nozzle clogging.

Graphical abstract

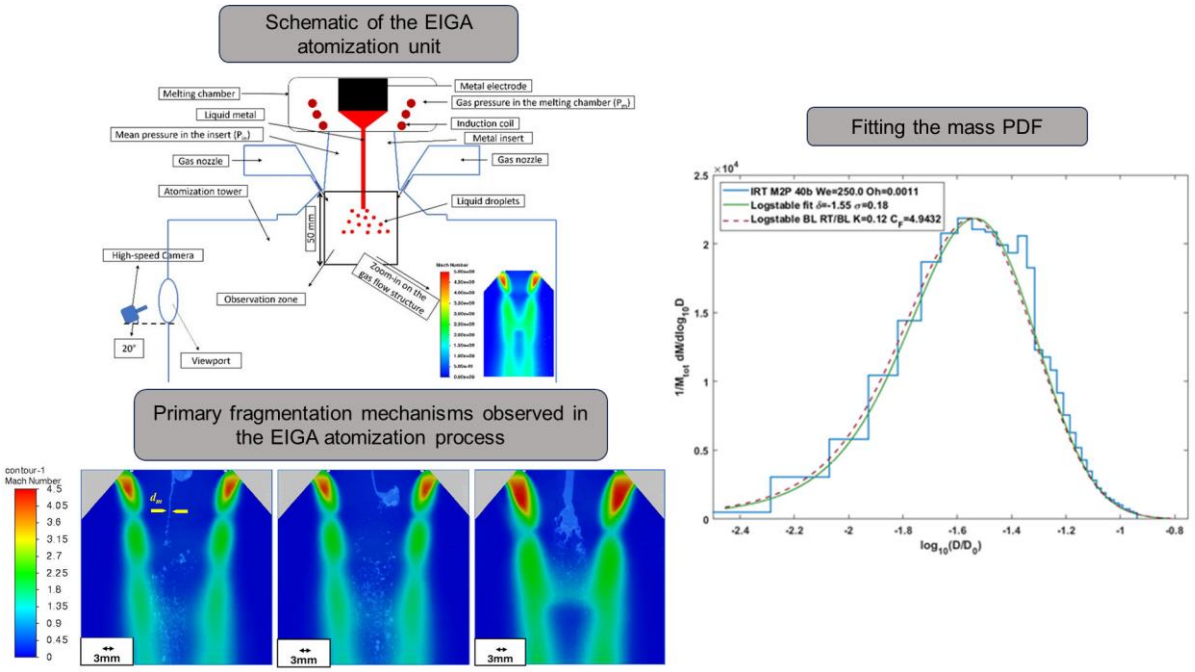

* Corresponding author: pierre.chapelle@univ-lorraine.fr

Abstract

Electrode Induction melting Gas Atomization (EIGA) is a free-fall gas atomization process used to produce metal powders, where a swirling supersonic gas jet hits a molten metal stream atomizing it into droplets through various fragmentation mechanisms. Fragmentation mechanisms of molten Ti64 are investigated by high-speed video visualization. The role of gas pressure and melting chamber overpressure on the fragmentation mechanisms and on the particle size distribution is determined. The mechanisms observed are fiber breakup, bag breakup and Rayleigh breakup for primary fragmentation and bag breakup and shear breakup for secondary fragmentation. Increasing the gas pressure promotes shear breakup and creates finer droplets. A model based on log-stable law is proposed to fit the mass distribution according to the dominant fragmentation regime. A good agreement is observed between the different analysis (dominant atomization regime, mass cumulative distribution evolution, parameters of log-stable law). A criterion for prediction of nozzle clogging is devised.

Keywords: Free-fall atomizer; swirling supersonic gas flow; metal powder; primary fragmentation; secondary fragmentation; high-speed camera.

1. Introduction

Over the last few years, the rapid growth of metal additive manufacturing in a large variety of industrial sectors (aeronautics, medical, automotive, etc.) has stimulated a strong demand for metal powders that meet very precise size distribution (i.e. narrow distribution and small particle median diameter) as well as high quality criteria (spherical, without porosity and without pollution). One of the most efficient techniques for producing these powders is gas atomisation, which is based on the fragmentation of a stream of molten metal by impact of a high-velocity jet of gas [1]. This study focuses on a specific gas atomisation technique, known as the EIGA (Electrode Induction melting Gas Atomization) process [2]. This process combines contactless melting of the lower tip of a vertical metal electrode using an induction coil and fragmentation of the molten metal in free fall by a supersonic jet of inert gas. Some systems, such as the one studied in this paper, feature a swirl motion imposed on the gas jet, with the aim of improving atomization efficiency by promoting interactions of the molten metal with a gas of higher kinetic energy [3]. Non-contact melting and atomization with an inert gas make the EIGA process very attractive for the production of high purity powders of reactive metals (such as titanium alloys, TiAl and precious metals). The size of the powders obtained is typically between 1 and 300 µm [4]. Compared with other gas atomization techniques (such as confined type gas atomizers), the EIGA process is less sensitive to freezing issues of the molten metal at the nozzle outlet, which makes it easier to operate. However, it is currently difficult to produce very fine powders using this process [5]. In order to influence the final particle size distribution of the powder and improve the yield of particles suitable for additive manufacturing technologies, a solid understanding of the fragmentation mechanisms of the molten metal would be greatly beneficial.

As the literature dedicated to the EIGA process remains scarce, actual knowledge of the physical details of the process is very limited. Several experimental studies explored and quantified the effects of the main operating parameters, such as the melt flow rate [6] and atomization pressure [7], on the powder characteristics (size distribution) and microstructure. In addition, the EIGA process was the subject of various modelling approaches. Some authors [8-11] focused on the simulation of the heating and melting process of the metal electrode with the help of multi-physics models. These models were used to study the deformation dynamics of the free surface of the liquid metal film at the electrode tip and the formation of the molten

stream. As far as the atomization process is concerned, Guo et al. [12] simulated the structure of the high velocity gas stream using a single-phase Computational Fluid Dynamics (CFD) model and confirmed the dominant role played by the atomization pressure. Zou and Xiao [13] reported a multiphase (gas-metal) model attempting to cover the whole atomization process. Their approach combined a Volume Of Fluid description of the deformation and pre-breakup process of discontinuous metal droplets and a Lagrangian particle tracking approach (coupled to a secondary breakup model) for the simulation of the evolution of the droplets formed after pre-breakup. More recently, the satellite formation mechanism under different pressures was investigated by Wu et al. [14] using an Euler-Lagrangian model. Their simulation results suggested that the increase in satellite content under high pressure was related to the larger and more intense gas recirculation zone. Although the above studies have been useful in characterizing the effects of important parameters (such as the atomization pressure) and gaining insights into the gas flow behaviour and particle trajectories, many aspects of the process are still not well understood. In particular, there is a critical need to study in more detail the gas and molten metal interactions and the fragmentation mechanisms.

For the fragmentation modelling itself, as there is a co-flow between the gas and the liquid, there is a clear analogy between the EIGA process and more classical air-blast atomizers. This process has been widely studied in the field of gas turbine design (*cf.* Lasheras and Hopfinder, [15]). While there have been some ongoing developments in this field (see Aliseda et al. [16] for instance), and recently by using X-ray imagery to look deeply into the fragmentation mechanism [17,18], overall, modelling remains scarce. This may explain why Zou and Xiao [13] or Mandal et al. [5] use very old modelling (like the TAB model [19] or the KHRT [20], *cf.* Ashgriz [21] for a review) in their work. In our opinion, the most interesting model of air-blast atomizer was developed by Varga et al. [22] and makes use of both the Kelvin Helmholtz instability model and the Rayleigh-Taylor instability but in two successive cascading steps. This model only gives some characteristic lengths and the shape of the Mass Distribution Function is still unknown. More recently, building on this modelling, Rimbert et al. [23] have devised a way of modelling the mass distribution function using log-stable laws. These laws seem to better represent the mass distribution than classical log-normal laws used, for instance, in the work of Jackiw and Ashgriz [24]. The main parameters governing the fragmentation processes are:

1) the Weber number, defined as

$$We = \rho_g U_r^2 d_m / \sigma \tag{1}$$

where ρ_g is the gas density, U_r is the relative velocity between the gas and the metal, d_m is the metal particle/drop diameter and σ is the surface tension of the gas-metal interface;

2) the Ohnesorge number, defined as

$$Oh = \frac{\mu_m}{\sqrt{d_m \rho_m \sigma}} \tag{2}$$

3) the viscosity ratio

$$\mu_R = \frac{\mu_m}{\mu_g} \tag{3}$$

4) the density ratio

$$\rho_R = \frac{\rho_m}{\rho_g} \tag{4}$$

The momentum flux ratio $M = \rho_g U_g^2 / \rho_m U_m^2$ is also used in the air-blast nozzle classification [15] but is often difficult to actually measure and is sometimes replaced by the gas to liquid surface ratio [25].

The aim of this work is to assist the development of a complete numerical model of the EIGA process that could provide eventually useful information to link the final properties of the obtained powders (mainly the particle size) with atomisation conditions. As a first step towards this goal, we have recently reported a numerical model of the gas flow dynamics that has allowed detailed investigation of the gas flow patterns for a wide range of operating conditions (e.g. gas pressure, gas nozzle slit width) [26]. The present paper focuses on the interactions between the gas and liquid metal phases and is an attempt to observe and identify the main phenomena that govern the fragmentation of the molten metal stream.

The paper is organized as follows. The interaction between the free-falling metal stream and the high-speed gas jet is investigated experimentally in a full scale EIGA facility via high-speed visualization experiments (section 2), from which various modes of metal fragmentation are described in detail (section 3.1). This study presents also an investigation of the impact of the gas pressure on the characteristics (size distribution) of the obtained powders (section 3.2) and it will be shown how the log-stable mass distribution model of Rimbert et al. [23] can be adapted to present results (section 3.3). Finally, a brief discussion regarding powder backflow and nozzle clogging issues encountered during the reported experiments is provided in section 3.4. Conclusions about the present work and their perspectives are presented in section 4.

2. Experimental setup

The present experimental work is performed in the EIGA facility (built by ALD Vacuum Technologies GmbH, Hanau, Germany) based at IRT M2P (Uckange, France), which is shown in Fig. 1. This atomization system mainly consists of a gas injection nozzle, a melting chamber and an atomization chamber. The gas injection nozzle is equipped with two tangential gas inlets of 12 mm diameter to produce a swirling motion of the gas flow. The gas flows with relatively homogeneous kinetic energy values through most of the nozzle and the gas flow regime remains subsonic [26]. The gas emerges from the nozzle through a converging annular gap with a width of 0.62 mm, resulting in a transition from a subsonic to a supersonic flow regime. Such a nozzle is responsible for the generation of a high velocity, high pressure gas jet forming a swirling supersonic gas flow in the atomization chamber. In the interior of the gas jet in the atomization chamber, Mach diamonds are produced with various dimensions and kinetic energies, as shown in the close-up view of the gas flow structure in Fig. 1 from the numerical simulation of the gas flow [26]. Argon is used as the inert gas inside the nozzle as this EIGA plant is implemented to produce reactive alloys (such as Ti alloys). A metal rod-shaped electrode in the melting chamber undergoes contactless melting in a conical induction coil. This type of non-contact induction melting limits any process-related pollution of the metal, allowing the production of ultra-clean powders, which makes the EIGA process particularly well suited to the manufacture of easily oxidized and highly reactive metal powders (such as titanium alloys). A stream of molten metal produced in the melting chamber flows vertically through a free fall nozzle and is impacted by the gas jet in the atomization chamber, breaking it into liquid droplets through various fragmentation mechanisms, which are transformed into metal powder particles after solidification. In this atomization system, the gas pressure in the

melting chamber is kept higher than the one in the atomizing chamber to prevent problems such as clogging and backflow of the metal droplets and to control the free-falling flow of the molten metal. To prevent strong variations of the pressure in the melting chamber and ensure that it remains within specified setpoints, it is adjusted throughout the entire atomization process using a PID controller. The molten metal stream is either a continuous flow or a discontinuous flow of drops [13] based on the electrode rotation and feeding velocity and the electrical power in the induction coil. This atomization tower is capable of atomizing electrodes with a maximum length of 1000 mm and three different diameters of 70, 100, and 150 mm, which corresponds to the production of about 15, 30, and 75 kg of Ti powders, respectively [4].

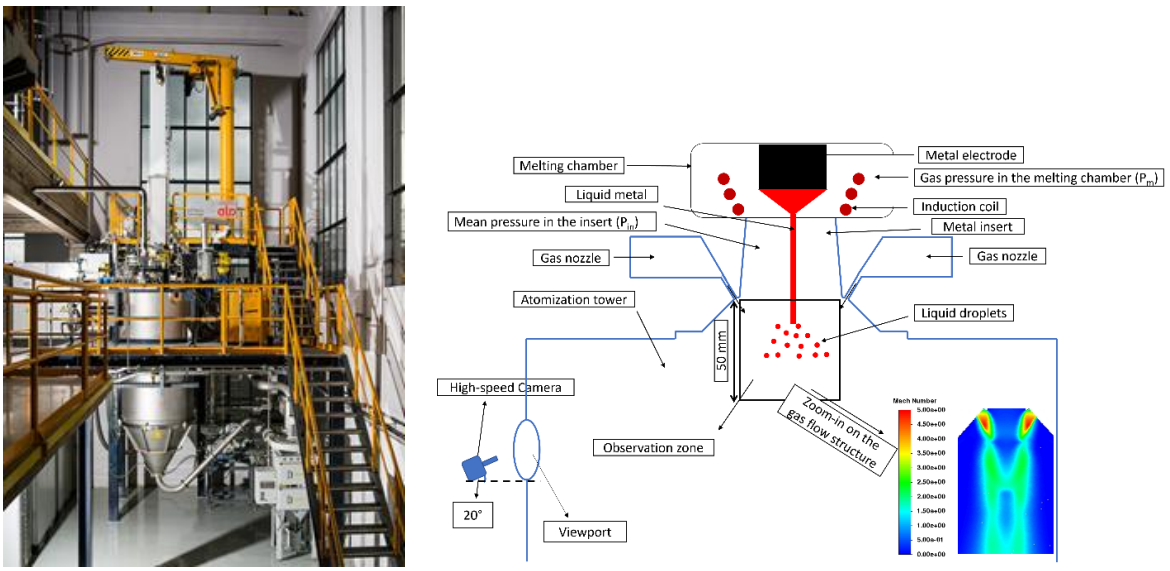

Fig. 1. Left: EIGA atomization unit at Uckange (France). Right: Schematic of the EIGA atomization unit showing the melting of the electrode and free fall of the liquid metal, its atomization into droplets, the installation of the high-speed video camera in front of a viewport, the observation region and a close-up view of the simulated gas flow structure in the observation region.

In order to identify and classify the different mechanisms of metal fragmentation within the EIGA process, the metal atomization is observed with a high-speed video camera placed in front of one the viewport of the EIGA tower (Fig. 1). The camera is tilted by 20° in order to better visualize the interest area downstream the nozzle exit. The observation region is 50 mm high and is located immediately underneath the gas nozzle. A close up view of the simulated gas flow pattern in the selected observation region, obtained using our gas flow numerical model [26], is shown in Fig. 1. It indicates the presence of several Mach diamonds inside the gas jet, which are expected to play an essential role on the fragmentation phenomena. The atomized metal is the titanium alloy Ti-6Al-4V (Ti64). The video camera used is a Photron SA-5 ultra-high-speed camera. The ISO setting is set to 10000 and the opening is set to 0.0625. The exposure time is 0.37 µs and the image acquisition rate is 25000 frames/s. The images obtained have a resolution of 0.097 mm/pixel. A Camsizer XT analyzer is used to measure the particle size distribution of the produced powder. The physical properties of argon and Ti64 liquid metal are listed in Table 1.

Table 1
Argon and Ti64 metal physical properties used in this study.

Physical properties	Density (kg/m^3)	Dynamic viscosity (Pa.s)	Surface tension (N/m)
Argon gas	1.76	$2.12 * 10^{-5}$	
Ti64 liquid metal	4500	$4.82 * 10^{-3}$	1.54

3. Results and discussion

As listed in Table 2, a total of 9 tests are performed on a Ti64 electrode of diameter 100 mm and length 700 mm using argon as atomizing gas. The role of the atomizing gas pressure at the nozzle inlet (between 5 and 40 bar) and the pressure in the melting chamber (between 1.04 and 1.3 bar) on the fragmentation mechanisms and on the particle size distribution of the produced powders is more particularly investigated in this study.

Table 2
Parameters of the tests performed.

Test no.	Gas pressure at the nozzle inlet (P_g) (bar)	Gas pressure in the melting chamber (P_m) (bar)	Nozzle outlet gap size (X) (mm)
#1	40	1.2	0.62
#2	30	1.2	0.62
#3	20	1.2	0.62
#4	10	1.2	0.62
#5	5	1.2	0.62
#6	30	1.04	0.62
#7	30	1.085	0.62
#8	30	1.1	0.62
#9	30	1.3	0.62

3.1. Visualization of liquid metal fragmentation modes

As a general rule, the fragmentation process is divided into two main stages. The first stage (referred to as primary fragmentation) is the disintegration of the molten metal stream to form ligaments and large fragments of liquid metal. Subsequently, in a second stage (referred to as secondary fragmentation), these primary structures fragments further into droplets of smaller sizes. As mentioned above, the actual understanding of the fragmentation phenomena in the specific context of the EIGA process is still limited. In order to interpret the observations and measurements reported in this paper, we will refer to the breakup phenomena described in the literature for other atomization systems. We will more particularly refer to the work of Zhao and Liu [25] which is an update of Lasheras and Hopfinger [15]. The main mechanisms listed for primary fragmentation by these authors are Rayleigh breakup, bag breakup, membrane fiber regime and fiber breakup. These mechanisms may be classified in a map depending on two parameters, namely the ratio of the gas-liquid nozzle exit area and the Weber number. Secondary fragmentation involves two main breakup modes: bag breakup and shear breakup. Bag breakup is usually thought to result from the Rayleigh-Taylor interfacial instability and comes in a variety of forms (bag breakup, bag-stamen breakup, dual-bag breakup, bag/plume breakup, multibag breakup…) as the Weber number increases. The shear breakup is mainly a consequence of the Kelvin-Helmholtz-like shear instability and occurs at high We values (usually above 80) [27].

All the fragmentation mechanisms observed during the performed trials are summarized in Table 4 located in section 3.4. Figs. 2–6 presented below illustrate examples of each primary and secondary fragmentation mechanism identified. For each mechanism, the high-speed camera image is superimposed on the gas flow structure map coloured by the gas flow Mach number (parameter expressing the ratio of the flow velocity to the sound velocity) obtained from the numerical model developed in [26]. A characteristic Weber number is also reported

for each mechanism in the legend of the figure. This Weber number was computed considering the diameter of the metal jet or drop measured from image processing at a given fragmentation instant with the Photron FASTCAM Viewer software and the local aerodynamic parameters (local velocity and density) of the gas determined from the numerical model developed in [26]. The velocity lag between the droplet and the gas is assumed close to the gas velocity as the droplet falling velocity is negligible. The mechanisms observed for primary fragmentation correspond to fiber breakup, bag breakup and Rayleigh breakup, whereas secondary fragmentation involves bag breakup, multibag breakup and shear breakup mechanisms.

The fiber breakup mechanism occurs when the gas pressure is the highest (40 bar) or the pressure in the melting chamber is low (≤1.1 bar). As observed in Fig. 2, it results in the rapid fragmentation of the metal stream into fine fiber-like structures. The gas energy in the core of the gas jet is high enough to cause the development of a Mach disk (i.e. normal shock wave in the space between the second Mach diamond). This mechanism is associated to a relatively large value of the Weber number ($We = 66$, $d_m = 3mm$).

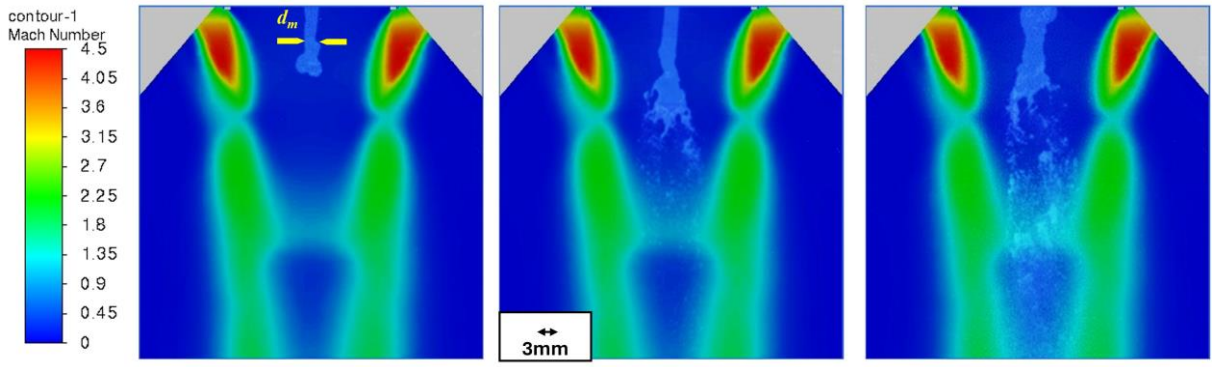

Fig. 2 . Primary fragmentation mechanism of fiber breakup ($We = 66$) observed in the EIGA atomization process. The video images are superimposed on the contour plot of the gas flow Mach number obtained from [26]. The gas flow calculation corresponds to case #1 in Table 2. $d_m = 3$ mm. The Weber number is computed in the subsonic (blue) region.

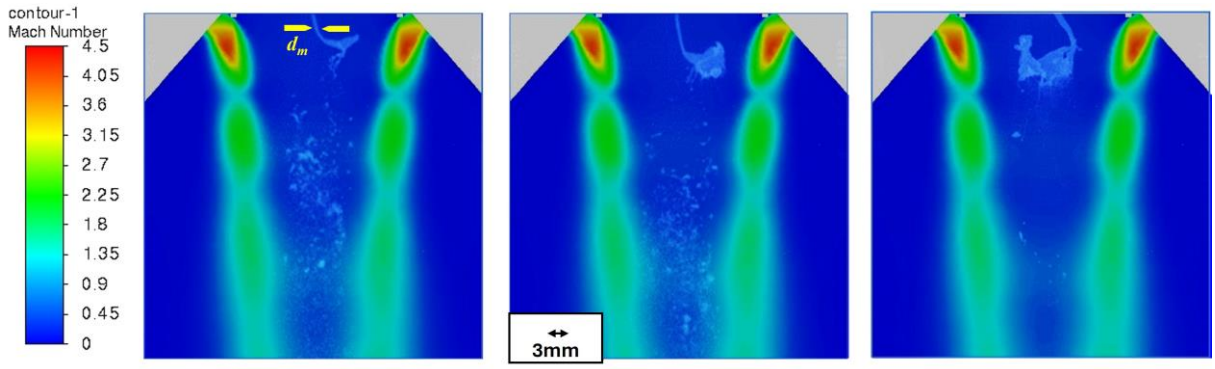

Fig. 3 . Primary fragmentation mechanism of bag breakup ($We = 14$) observed in the EIGA atomization process. The video images are superimposed on the contour plot of the gas flow Mach number obtained from [26]. The gas flow calculation corresponds to case #2 in Table 2. $d_m = 0.7$ mm.

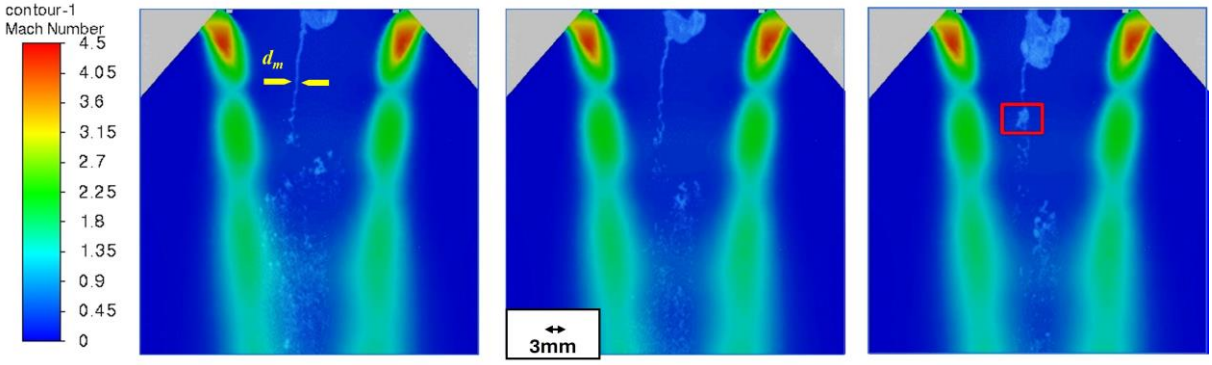

Fig. 4 . Primary fragmentation mechanism of Rayleigh breakup ($We = 8$) observed in the EIGA atomization process. The video images are superimposed on the contour plot of the gas flow Mach number obtained from [26]. The gas flow calculation corresponds to case #2 in Table 2. $d_m = 0.35$ mm. The red box shows a drop undergoing bag type breakup.

The Rayleigh breakup and bag breakup mechanisms are observed under lower atomization gas pressure levels (pressure range of 20-30 bar) or higher-pressure levels in the melting chamber (≥1.2 bar). In these modes, the breakup is driven by surface wave instabilities. Bag breakup is generated when the jet stretches into a thin sheet and involves the growth of Rayleigh-Taylor waves on the front forming a hollow bag that fragments into small droplets. The metal stream diameter is smaller ($d_m = 0.7$ mm) compared to the fiber breakup case ($d_m = 3$ mm). Hence, the metal stream is more influenced by the gas, thus swirling with the gas flow. Rayleigh breakup fragmentation is related to the Rayleigh-Plateau type instability. In this mode, the diameter of the metal jet is the thinnest ($d_m = 0.35$ mm) and the formed droplets are almost twice larger, resulting in a fragmentation of bag breakup mechanism in the secondary fragmentation (see red rectangle in Fig. 4). Fiber breakup requires about 1 ms to initiate shearing of liquid metal volume. On the other hand, in the case of the bag breakup and Rayleigh breakup mechanisms, because of the stronger fluctuations of the metal sheet induced by the gas flow, the metal stream fragments much more quickly (in less than 0.2 ms). For the low pressures at 10 and 5 bar (tests #4 and #5 in Table 2), no primary fragmentation mechanisms were observed, as it appears that the metal jet underwent primary fragmentation in the region above the selected observation region.

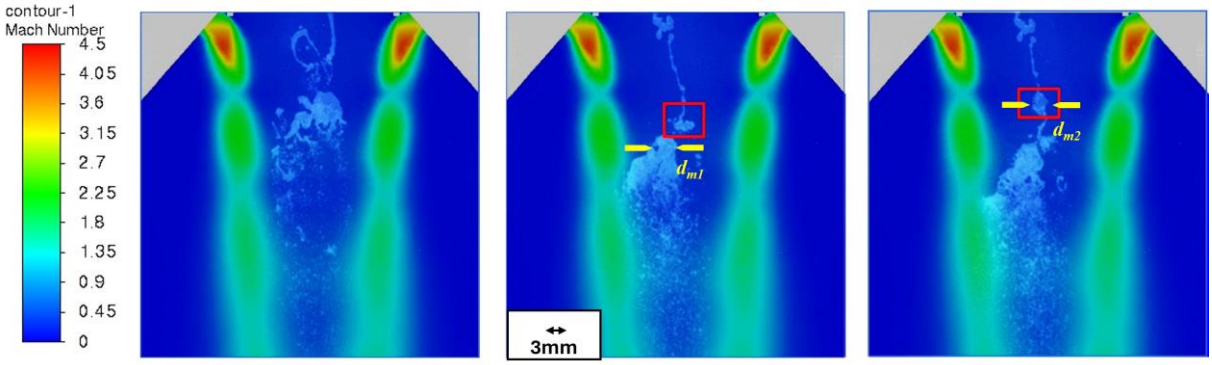

Fig. 5 . Secondary fragmentation mechanisms of shear breakup ($We = 90$) and bag breakup ($We = 15$) observed in the EIGA atomization process. The video images are superimposed on the contour plot of the gas flow Mach number obtained from [26]. The gas flow calculation corresponds to case #2 in Table 2. $d_{m,1} = 3$ mm for shear breakup and $d_{m,2} = 0.6$ mm for bag breakup. The red box shows a drop undergoing bag type breakup.

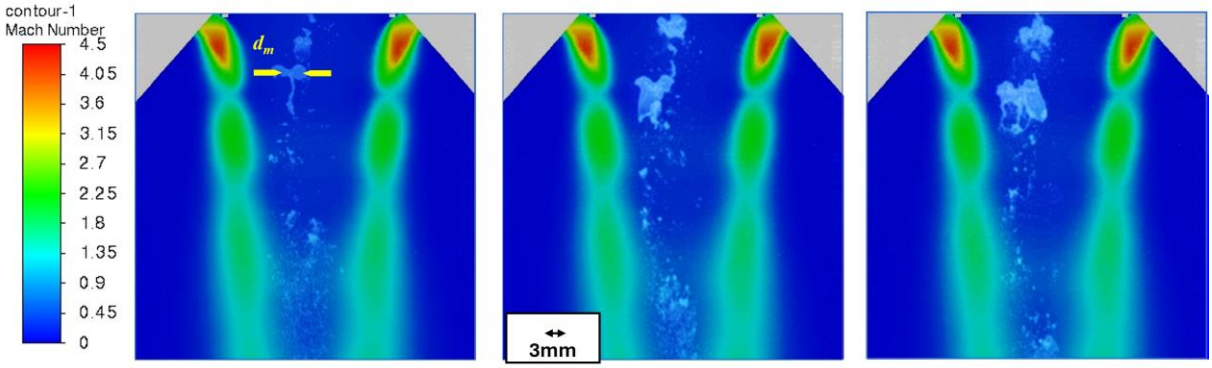

Fig. 6. Secondary fragmentation mechanism of multibag breakup ($We = 60$) observed in the EIGA atomization process. The video images are superimposed on the contour plot of the gas flow Mach number obtained from [26]. The gas flow calculation corresponds to case #2 in Table 2. $d_m = 3\text{mm}$.

The same secondary fragmentation mechanisms (i.e. bag breakup, multibag breakup and shear breakup) were observed in all the tests performed except for the highest atomization pressure (40 bar) and the low pressure in the melting chamber (≤1.1 bar). For bag breakup, the metal drop deforms into a disc, then into a bag which rapidly fragments into tiny droplets (time scale of about 0.3 ms). In the multibag breakup mode, the surface of the bag has several lobes which burst one after the other (time scale of about 0.4 ms). During the shear breakup mode, the metal drop approaches very close to the most energetic gas region (Mach diamond) leading to its disintegration into droplets under a shear effect caused by the gas flow. The estimated Weber number varies between 10-40 for bag breakup, 40-60 for multibag breakup and is superior to 60 for shear breakup. These results agree with previous studies ([28-31]…etc.) on secondary breakup and recent studies on airblast atomizer [32].

3.2. Global atomization performance and cumulative mass size distribution analysis

The effect of the gas pressure at the nozzle inlet on the particle size distribution of the obtained powder is studied from the results of tests #1, #2 and #3 in Table *2*. Because the minimum operative pressure applied in the real atomization process is at 20 bar, the particle size distribution for lower pressures is not discussed in this section (tests #4 and #5). Fig. 7 compares the cumulative particle size distribution measured for these three tests. The particle diameters corresponding to the 10^{th}, 50^{th} and 90^{th} percentiles of these distributions are reported in Table 3. An increase in the atomizing gas pressure from 20 to 30 bar favors the production of fine powders, resulting in a decrease of the mass median particle diameter (d50 or MMD) by 17 %, and an increase of the percentage of the powder suitable for additive manufacturing (< 63 µm) by about 26 %. An increase in the gas pressure from 30 to 40 bar reduces the median particle diameter by 9 % and improves the percentage of powder suitable for additive manufacturing (< 63 µm) by about 17 %. These results are due to the overall increase in gas velocity, and thus of its kinetic energy, when increasing the atomizing gas pressure, which results in the formation of finer droplets. This trend is consistent with the evolution of the breakup regime observed experimentally in Section 3.1. From these observations, under the different gas pressure investigated, the secondary breakup mechanisms are similar, whereas several primary breakup mechanisms exist. Low gas pressures (20-30 bar) are associated to a Rayleigh breakup / bag breakup regime, whereas a fiber breakup regime occurs for large gas pressure (40 bar). As a rule, the droplet size resulting from fiber breakup is expected to be much smaller than that produced by Rayleigh breakup and bag breakup, which agrees with the effect of the gas pressure on the particle size distribution observed in Fig. 7.

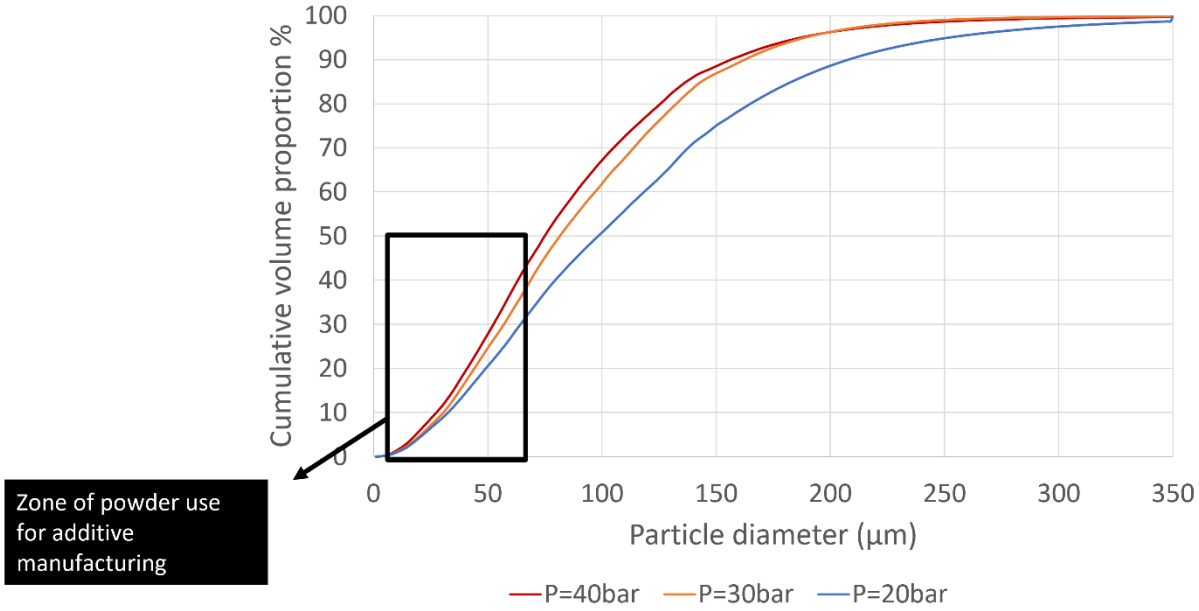

Fig. 7. Cumulative volume proportion versus powder diameter for three different atomization pressures.

Table 3
Comparison of the 10th, 50th and 90th percentiles of the cumulative distribution measured for different atomization conditions. Note that d50 is also often referred to as Mass Median Diameter or MMD.

Test no.	Gas pressure at the nozzle inlet (P_g) (bar)	Gas pressure in the melting chamber (P_m) (bar)	Nozzle outlet gap size (X) (mm)	d10 (µm)	d50 or MMD (µm)	d90 (µm)
#1	40	1.2	0.62	27	75	156
#2	30	1.2	0.62	30	82	162
#3	20	1.2	0.62	32	98	207
#8	30	1.1	0.62	28	81	180
#9	30	1.3	0.62	33	94	198

The effect of different levels of gas overpressure (ΔP) in the melting chamber of the metal electrode on the final particle size obtained is studied from the results of tests #2, #8 and #9 in Table *2*. Due to the clogging of the nozzle during tests #6 and #7 in Table *2*, their results are not presented here. Fig. 8 compares the cumulative volume ratio for three different melting chamber pressures. The particle diameters corresponding to the 10th, 50th and 90th percentiles of these distributions are reported in Table 3. Decreasing the melting chamber pressure from 1.3 to 1.2 bar favors the production of fine powders, decreases the Mass Median Diameter (d50 or MMD) by 14% and increases the percentage of powder suitable for additive manufacturing (<63 µm) by 29%. A reduction in melting chamber pressure below 1.2 bar has only a small impact on particle size distribution. Although it does not show a major influence on the average particle diameter, it shows nevertheless a slight increase of very fine particles (< 63 µm). Again, such an evolution of the particle size distribution agrees with the primary breakup behavior observed by high-speed imaging in Section 3.1. Indeed, as the melt chamber overpressure decreases, the primary breakup mechanism changes from a Rayleigh breakup / bag breakup regime to a fiber breakup regime. As mentioned above, this latter regime involves the production of smaller size particles than the first two regimes (which is consistent with the evolution of the particle size distribution observed in Fig. 8). Note that, similarly to the effect of

the gas atomization pressure, the variations in the melt chamber overpressure considered in our study have very little impact on the secondary breakup mechanisms.

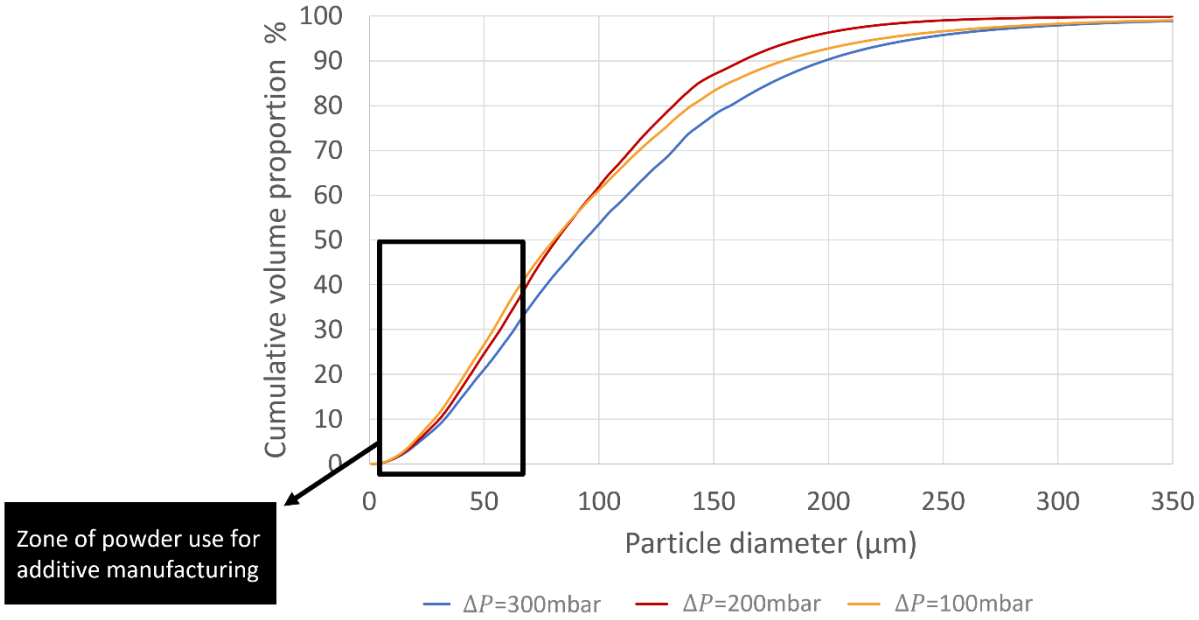

Fig. 8. Cumulative volume proportion versus powder diameter for three different pressures between the melting and the atomization chambers.

3.3. Mass log stable distribution and detailed fragmentation mechanisms

In order to model further the mass distribution, Rimbert and Séro-Guillaume [33] introduced log-stable laws as a generalization of widely used log normal laws. This work is a generalization of Kolmogorov's [34] work on asymptotic solution of the fragmentation equation which had been modernized by Novikov and Dommermuth [35], using log infinitely divisible distribution and continuous time process by Gorokhovski and Saveliev [36]. The main modification of Rimbert and Séro-Guillaume [33] was to consider mass distribution instead of number distribution and to select among the log infinitely divisible distributions by only considering log-stable laws. The Lévy stable laws are given analytically by their characteristic function $\hat{p}_\alpha$ (*i.e.* the Fourier transform of their PDF) which take the form:

$$\hat{p}_\alpha(k;\beta,\lambda,\delta) = \exp\left(ik\delta - \lambda^\alpha |k|^\alpha \left[1 + i(sign(k))\beta\omega(|k|,\alpha)\right]\right) \tag{5}$$

where

$$\omega(|k|,\alpha) = \begin{cases} \tan(\alpha\pi/2) & \text{if } \alpha \neq 1 \\ -(2/\pi)\log|k| & \text{if } \alpha = 1 \end{cases} \tag{6}$$

and α ($0 < \alpha \leq 2$) is the stability index governing the decrease of the tail of the probability, λ ($\lambda > 0$) is the scale parameter, analogous to the standard deviation of the normal law, and δ, a real number, is the shift parameter governing the mean of the distribution. β ($-1 \leq \beta \leq 1$) is a

"skewness" (different from traditional skewness) parameter, $\beta = 0$ indicates a symmetric distribution, $\beta < 0$ a distribution skewed to the left and $\beta > 0$ a distribution skewed to the right. One can notice that if $\alpha = 2$, the distribution is Gaussian and the parameter β is meaningless since $\omega(|k|,\alpha) = 0$ (normal distributions are not skewed). When β = -1 the distribution is said totally skewed to the left and all positive moments of the log-stable distribution are finite. Rimbert et al. [23] present a full model that allow the determination of all four parameters. It is based on a "two steps" cascading instability mechanism. The ratio between different length scales gives some parameters of the distribution. To summarize:

- $\alpha = 1.7$ (an explanation of this value can be found in [37])
- $\beta = -1$
- $\lambda = \log_{10}\left(\frac{\lambda_{RT}}{\lambda_{shear}}\right)$
- $\delta = \log_{10}\left(\frac{\lambda_{shear}}{d_m}\right)$

Where λ_{shear} is the wavelength of the shear (Kelvin-Helmholtz like) instability given by:

$$\frac{\lambda_{shear}}{d_m} = \frac{2\pi}{0.4}\left(1+\frac{\rho_R^{1/3}}{\mu_R^{1/3}}\right)\left(1+\left(\rho_R\mu_R\right)^{1/3}\right)^{1/2}\frac{K}{\sqrt{\mathrm{Re}_m}} \tag{7}$$

ρ_R is the metal to gas density ratio (here close to 2556) and μ_R is the metal to gas dynamic viscosity ratio (here close to 227), K is a (geometric) boundary layer development coefficient ($K \approx 0.5$ for jet breakup) and $Re_m = \rho_m U_r d_m / \mu_m$ is the metal Reynolds number.

$$\frac{\lambda_{RT}}{d_m} = \pi\sqrt{\frac{8}{C_F We}}\sqrt{\frac{d_m}{\lambda_{shear}}} \tag{8}$$

C_F is a friction coefficient governing the late stage (Rayleigh-Taylor instability) of the droplet fragmentation ($C_F \approx 3$ for jet breakup). Fig. 9 shows an application of this modelling to the present results. Two cases are presented here. Case #1 which has been shown to be dominated by shear breakup and case #2 which present a combination of bag and shear breakups. In both case the mass distribution seems to be adequately fitted with a log-stable law. Considering the proposed model, it also seems to be valid but needs a new fitting of the parameters C_F and K for the two proposed cases. Moreover, it was needed for case #1 to compute the Weber number in the supersonic region present on the vertical axis (Mach diamond, *cf.* Fig. 2). Therefore, the value $We = 250$ has been used in this case. Note also that the resulting mass PDF is computed on about two minutes of atomization process and corresponds to many different breakup events (video recording corresponds to roughly 3 s of the process to compare with). Therefore, this Weber number should actually be considered as an average Weber number. Now, if we look at its definition, we can assume that:

$$\langle We\rangle = \left\langle\frac{\rho_g U_r d}{\sigma}\right\rangle \approx \frac{\rho_g}{\sigma}\langle U_r d\rangle \approx \frac{\rho_g}{\sigma}\langle U_g d\rangle \approx \frac{\rho_g}{\sigma}\langle U_g\rangle\langle d\rangle \tag{9}$$

where $\langle\bullet\rangle$ stands for the classical statistical average and where we have assumed that the properties of gas density and the surface tension were identical for every fragmentation event

(but this is approximate, surface tension may change slightly when the droplet cools down for instance…*etc.*). Moreover, we assumed that the velocity difference is very close to the gas velocity which is considered independent from the droplet size. Therefore, the average droplet size $\langle d \rangle \approx d_m$ can also be considered as a fitting parameter (except that it has been fixed using image analysis). Note also that this consideration could be extended to the other non-dimensional numbers of the modelling (*i.e.* Reynolds number, viscosity and density ratio).

For case #1, which is the highest available gas pressure Pg, the dominant fragmentation mechanism is shear breakup (there are almost no bag breakup). For case #2, the supersonic zone on the axis is barely present and this may explain why a mixture of bag and shear breakup has been observed in this case. There is also an important variation of the parameter K between the two cases, which is close to 0.12 for case #1 (shear breakup) and close to 0.34 for case #2 (bag breakup) while the friction coefficient C_F has been set to 4.9 for case #1 and 2.8 for case #2. This agrees with finer droplets obtained in case #1 as seen previously (*cf.* fig.7 for instance). Note again that both estimates of d_m and We are very important when fitting these parameters and that some complementary analysis would be needed to comfort the proposed coefficient values (like determining the exact mixture ratio between bag and shear breakup). Lastly, it can be seen that the model is sensitive to both the viscosity ratio and density ratio of the gas, which are somewhat unknown (superheat is not measured for instance) and the liquid which also introduces *de facto* some uncertainty on the coefficients.

Let us note that in spite of these remaining open questions, a fitting by a log-stable law is always possible (as can be seen on fig. 9). However, in order to get really predictive results, further investigations are needed.

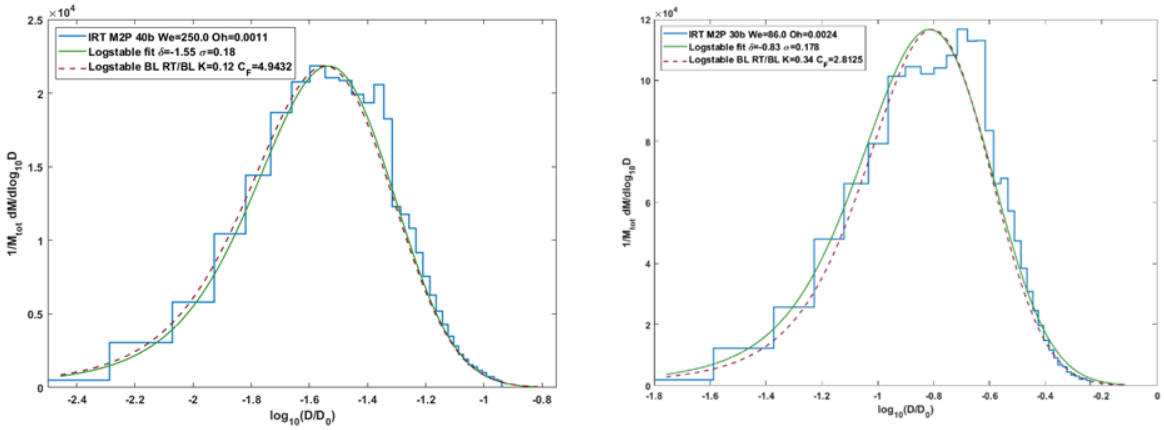

Fig. 9. Fitting the mass PDF: On the left, case #1, $d_m = D_0 = 3\ mm$ (and 63 microns stand for -1.67), on the right, case #2 $d_m = D_0 = 0.6\ mm$ (and 63 microns stand for -0.98).

3.4. Powder backflow and nozzle clogging

During the tests performed #2, #6, #7 and #8 in Table *2*, the atomization process was disturbed by some backflow of powder particles towards the melting chamber, and in two cases the nozzle clogged. The nozzle clogging phenomenon in a close-coupled atomization process has already been reported in several papers [38,39], but has not yet been observed in free-fall atomization. In order to understand the cause of such phenomenon, the average gas pressure and the average Weber number (considering the molten metal stream diameter to be equal to 5 mm) in the insert region (i.e. conical volume directly below the melt delivery nozzle, cf. Fig. 1b) were calculated by means of the gas flow model described in [26]. The results of these calculations are presented in Table 4 for 7 of the 9 tests performed.

Table 4
Summary of the fragmentation mechanisms observed during the trials and calculation of the averaged Weber number for a particle diameter equal to 5mm and the average gas pressure in the insert region.

Test no.	P_g (bar)	P_m (bar)	X (mm)	Comments	Primary fragmentation	Secondary fragmentation	d50 or MMD (µm)	Mean Weber number in the insert	Mean pressure in the insert (P_{in}) (bar)	Ratio P_{in}/P_m
#1	40	1.2	0.62	Powders backflow in the melting chamber	Fiber breakup	Shear breakup and Bag breakup	75	60	1.084	0.9
#2	30	1.2	0.62	-	Bag breakup and Rayleigh breakup	Shear breakup, multibag breakup and Bag breakup	82	86	1.026	0.855
#3	20	1.2	0.62	-	Bag breakup and Rayleigh breakup	Shear breakup, multibag breakup and Bag breakup	98	101	0.99	0.825
#4	10	1.2	0.62	-	-	Shear breakup, multibag breakup and Bag breakup	-	-	-	-
#5	5	1.2	0.62	-	-	Shear breakup, multibag breakup and Bag breakup	-	-	-	-
#6	30	1.04	0.62	Nozzle clogging	Fiber breakup	Shear breakup and Bag breakup	-	44	0.955	0.92
#7	30	1.085	0.62	Nozzle clogging	Fiber breakup	Shear breakup and Bag breakup	-	52	0.988	0.91
#8	30	1.1	0.62	Powders backflow in the melting chamber	Fiber breakup	Shear breakup and Bag breakup	81	58	0.99	0.9
#9	30	1.3	0.62	-	Bag breakup and Rayleigh breakup	Shear breakup, multibag breakup and Bag breakup	94	114	1.062	0.817

These results reveal the following trends: An increase in the pressure P_g of the atomizing gas and/or a decrease in the overpressure P_m in the melting chamber results in an increase of the pressure P_{in} of the gas in the insert region (*cf.* fig. 1), as well as a decrease of its kinetic energy (therefore the Weber number decreases). These two effects on the gas parameters in the

insert region (the increase of the gas pressure and the decrease of the gas kinetic energy) contribute to the degradation of the fragmentation conditions in the upper part of the tower and may explain the observed evolution of the primary fragmentation mechanism from bag breakup / Rayleigh breakup to fiber breakup, as well as the observed phenomenon of powder backflow. As far as the gas pressure in the insert is concerned, its increase leads to a situation where the pressure in the insert is very close to the pressure in the melting chamber, reducing the aspiration of the metal stream and thus increasing the risk of particle backflow and nozzle clogging. Moreover, the reduction of the metal stream aspiration, in the same way as the decrease of the gas kinetic energy in the insert region, has a negative impact on the primary fragmentation of the metal in the insert region. It results in a larger metal jet diameter (d_m = 3 mm at 40 bar vs. d_m = 0.7 mm at 30 bar) leading to the interaction of a larger volume of liquid with the Mach diamonds and thus promoting the fragmentation into fibers. The fiber breakup fragmentation results eventually in the violent release of a large number of metal fragments (including a large proportion of very fine droplets), which are projected in all directions and may potentially lead to some backflow.

It is worth noting that the onset of powder backflow and nozzle clogging seems to be controlled by a threshold value of the ratio of the average pressure in the insert to the pressure in the melting chamber. Powder backflow is observed when the value of this ratio approaches 0.9, while nozzle clogging is observed when this ratio exceeds 0.9.

4. Conclusion

To conclude, in this work, experimental results on the different fragmentation mechanisms found in an EIGA tower when the atomization gas pressure is varied have been reported. The primary breakup mechanisms are closely related to known air blast atomization mechanisms (Rayleigh breakup, bag breakup, membrane and fiber or fiber breakup) while secondary atomization mechanisms are either of the bag breakup (kind for the lower atomization gas pressure) or of the shear breakup kind. Note that for the higher atomization gas pressure, the fiber breakup principally happens when the primary liquid crosses the Mach disk where the velocity lag between the droplet and the gas is maximum which leads to the higher Weber number. This mode is dominant and promotes fine droplets.

Therefore, in the present work, the EIGA apparatus' best performance are obtained for a feeding pressure of Argon of 40 bar. This can be clearly seen when comparing the different cumulative mass distribution. To look further into the detail, a new model to compute the mass distribution is discussed and seems promising as it explains why previous CFD modelling [13,14] cannot reproduce the observed mass PDF as the modelling they use does not contain the adequate physics. However, this modelling part is far from complete partly due to the inhomogeneity of the gas flow, to variations in the liquid pouring due to unperfect control of the inductive melting and uncertainty on the physical properties of both the gas (due to the inhomogeneity) and the melt (due to the lack of knowledge of the initial temperature of the melt and since no cooling model has been introduced yet). Therefore, a more detailed fragmentation and solidification model should be devised and implemented in a CFD software. From the experimental point of view, part of this work will involve automatically sorting the different fragmentation mechanisms through image analysis to improve the computation of the statistics of the different parameters (like mode and location of a breakup event, computation of the local viscosity ratio, density ratio as well as the Weber and Reynolds numbers). This is however left for future work.

Last, when the pressure difference between the melting chamber and the insert is slight, it has been seen that clogging of the nozzle can happen. Actually, this can be quantified and when the pressure ratio P_{in}/P_m is superior to 0.9, clogging has been occurring and this is proposed as a clogging criterion for the present apparatus.

CRediT authorship contribution statement

Baraa Qaddah: Conceptualization, Investigation, Methodology, Formal analysis, Writing – original draft. **Pierre Chapelle:** Conceptualization, Methodology, Writing – original draft. **Jean Pierre Bellot:** Conceptualization, Supervision. **Julien Jourdan:** Investigation, Methodology. **Gagan Kewalramani:** Formal analysis. **Agathe Deborde:** Conceptualization, Supervision. **Raphael Hammes:** Investigation. **Nicolas Rimbert:** Conceptualization, Investigation, Methodology, Formal analysis, Writing – original draft.

Declaration of Competing Interest

The authors declare that they have no known competing financial interests or personal relationships that could have appeared to influence the work reported in this paper.

Acknowledgements

IRT M2P acknowledges the support of the French “Investissements d’Avenir” Program (ref. ANR-10-AIRT-04) within the framework of the SIGMA project. The authors also thank everyone at MetaFensch and IJL involved in the experimental trials.

References

[1] A.J. Yule, J.J. Dunkley, Atomization of Melts for Powder Production and Spray Deposition, Oxford University Press, 1994.

[2] M. Hohmann, N. Ludwig N., 1991. German patent - DE 4102101 C2.

[3] M. Haghighatjoo, A numerical investigation of free-fall swirling gas atomization process, MSc Thesis, Concordia University, Montréal, Canada, 2020.

[4] A. Deborde, N. McDonald, Atomisation de poudres d’alliages de titane, Traitements & Matériaux 458 (2019) 31–36 (in french), https://traitementsetmateriaux.fr/atomisation-de-poudres-dalliages-de-titane.

[5] S. Mandal, A. Sadeghianjahromi, C.C. Wang, 2022. Experimental and numerical investigations on molten metal atomization techniques – A critical review. Advanced Powder Technology. 33, 103809. https://doi.org/10.1016/j.apt.2022.103809.

[6] R. Gerling, M. Hohmann, F.P. Schimansky, Gas atomization of high melting reactive metals by a crucible and ceramic-free technique, Mater. Sci. Forum 539–543 (2007) 2693-2698. https://doi.org/10.4028/www.scientific.net/MSF.539-543.2693.

[7] K.K. Guo, C.S. Liu, S.Y. Chen, H.H. Dong, S.Y. Wang, High pressure EIGA preparation and 3D printing capability of Ti-6Al-4V powder, Trans. Nonferrous Met. Soc. China 30 (2020) 147-159. https://doi.org/10.1016/S1003-6326(19)65187-3.

[8] V. Bojarevics, A. Roy, K. Pericleous, Numerical model of electrode induction melting for gas atomization, COMPEL-Int. J. Comput. Math. Electr. Electron. Eng. 30 (2011) 1455-1466. http://www.emeraldinsight.com/0332-1649.htm.

[9] S. Spitans, H. Franz, E. Baake, Numerical modelling and optimization of the electrode induction melting for inert gas atomization (EIGA), Metallurgical and Materials Transactions B 51 (2020) 1918. https://doi.org/10.1007/s11663-020-01934-5.

[10] H. Li, Y. Shen, P. Liu, W. Liang, M. Wang, S. Wang, 2021. Multi-physics coupling simulation of electrode induction melting gas atomization for advanced titanium alloys powder preparation. Nature Scientific Report. 11, 23106. https://doi.org/10.1038/s41598-021-02316-w.

[11] B. Zhao, M. Xia, J.F. Wang, C.C. Ge, 2022. Numerical simulation and experimental study on production of high-speed steel powder by high-frequency induction melting gas atomization. Metall. Res. Technol.. 119, 509. https://doi.org/10.1051/metal/2022030.

[12] K. Guo, C. Liu, S. Chen, J. Li, Q. Fu, 2017. Effect of atomization pressure on the flow field distribution of TC4 alloy powder prepared by EIGA. IOP Conf. Series: Materials Science and Engineering. 207, 012046. https://iopscience.iop.org/article/10.1088/1757-899X/207/1/012046.

[13] H. Zou, Z. Xiao, 2021. Pre-breakup mechanism of free-fall nozzle in electrode induction melting gas atomization. Materials Today Communication. 29, 102778. https://doi.org/10.1016/j.mtcomm.2021.102778.

[14] J. Wu, M. Xia, J. Wang, B. Zhao, C. Ge, 2023. Effect of electrode induction melting gas atomization on powder quality: Satellite formation mechanism and pressure. Materials. 16, 2499. https://doi.org/10.3390/ma16062499.

[15] J.C. Lasheras, E.J. Hopfinger, Liquid jet instability and atomization in a coaxial gas stream, Annual Review of Fluid Mechanics 32 (2000) 275-308. https://doi.org/10.1146/annurev.fluid.32.1.275.

[16] A. Aliseda, E.J. Hopfinger, J.-C. Lasheras, D.M. Kremer, A. Berchielli, E.K. Connolly, Atomization of viscous and non-Newtonian liquids by a coaxial, high-speed gas jet. Experiments and droplet size modeling, International Journal of Multiphase Flow 34 (2008) 161-175. https://doi.org/10.1016/j.ijmultiphaseflow.2007.09.003.

[17] N. Machicoane, J.K. Bothell, D. Li, T.B. Morgan, T.J. Heindel, A.L. Kastengren, A. Aliseda, Synchrotron radiography characterization of the liquid core dynamics in a canonical two-fluid coaxial atomizer, International Journal of Multiphase Flow 115 (2019) 1-8. https://doi.org/10.1016/j.ijmultiphaseflow.2019.03.006.

[18] J.K. Bothell, N. Machicoane, D. Li, T.B. Morgan, A. Aliseda, A.L. Kastengren, T.J. Heindel, 2020. Comparison of X-ray and optical measurements in the near-field of an optically dense coaxial air-assisted atomizer. International Journal of Multiphase Flow. 125, 103219. https://doi.org/10.1016/j.ijmultiphaseflow.2020.103219.

[19] P.J. O'Rourke, A.A. Amsden, 1987. The TAB method for numerical calculation of spray droplet breakup. SAE technical paper. No. 872089. https://doi.org/10.4271/872089.

[20] M.A. Patterson, R.D. Reitz, Modeling the effects of fuel spray characteristics on diesel engine combustion and emission, SAE transactions 107 (1998) 27-43. https://doi.org/10.4271/980131.

[21] N. Ashgriz, Handbook of Atomization and Sprays, Springer, 2011.

[22] C.M. Varga, J.C. Lasheras, E.J. Hopfinger, Initial breakup of a small-diameter liquid jet by a high-speed gas stream, Journal of Fluid Mechanics 497 (2003) 405-434. https://doi.org/10.1017/S0022112003006724.

[23] N. Rimbert, M. Hadj-Achour, B. Ji, G. Kewalramani, A. Labergue, Y. Dossmann, M. Gradeck, P. Piluso, R. Meignen, 2023. Mass log-stable distribution of fragments in liquid–liquid jet fragmentation based on a two-step cascade between viscous shear instability and Rayleigh–Taylor instability. International Journal of Multiphase Flow. 167, 104518. https://doi.org/10.1016/j.ijmultiphaseflow.2023.104518.

[24] I. Jackiw, N. Ashgriz, 2023. Aerodynamic droplet atomization model (ADAM). Journal of Fluid Mechanics. 958, A2. https://doi.org/10.1017/jfm.2022.1046.

[25] H. Zhao, H. Liu, Environmental Impact of Aviation and Sustainable Solutions: Breakup Morphology and Mechanisms of Liquid Atomization. IntechOpen, 2020. https://www.intechopen.com/chapters/66460.

[26] B. Qaddah, P. Chapelle, J.-P. Bellot, J. Jourdan, N. Rimbert, A. Deborde, R. Hammes, A. Franceschini, 2023. Swirling supersonic gas flow in an EIGA atomizer for metal powder production: Numerical investigation and experimental validation. Journal of Material Processing Technology. 311, 117814. https://doi.org/10.1016/j.jmatprotec.2022.117814.

[27] M. Jain, R.S. Prakash, G.Tomar, R.V. Ravikrishna, 2015. Secondary breakup of a drop at moderate Weber numbers. Proc. R. Soc. A. 471, 20140930. https://doi.org/10.1098/rspa.2014.0930.

[28] M. Pilch, C.A. Erdman, Use of breakup time data and velocity history data to predict the maximum size of stable fragments for acceleration-induced breakup of a liquid drop, International Journal of Multiphase Flow 13 (1987) 741-757. https://doi.org/10.1016/0301-9322(87)90063-2.

[29] W.H. Chou, L.P. Hsiang, G.M. Faeth, Temporal properties of drop breakup in the shear breakup regime, International Journal of Multiphase Flow 23 (1997) 651-669. https://doi.org/10.1016/S0301-9322(97)00006-2.

[30] W.H. Chou, G.M. Faeth, Temporal properties of secondary drop breakup in the bag breakup regime, International Journal of Multiphase Flow 24 (1998) 889-912. https://doi.org/10.1016/S0301-9322(98)00015-9.

[31] Z. Dai, G.M. Faeth, Temporal properties of secondary drop breakup in the multimode breakup regime, International Journal of Multiphase Flow 27 (2001) 217-236. https://doi.org/10.1016/S0301-9322(00)00015-X.

[32] N. Machicoane, R. Osuna-Orozco, A. Aliseda, 2023. Regimes of the length of a laminar liquid jet fragmented by a gas co-flow. International Journal of Multiphase Flow. 165, 104475. https://doi.org/10.1016/j.ijmultiphaseflow.2023.104475.

[33] N. Rimbert, O. Séro-Guillaume, 2004. Log-stable laws as asymptotic solutions to a fragmentation equation: application to the distribution of droplets in a high Weber-number spray. Physical Review E. 69, 056316. https://journals.aps.org/pre/abstract/10.1103/PhysRevE.69.056316.

[34] A.N. Kolmogorov, On the lognormal distribution law of the dimensions of particles under pulverization, Doklady of the Akademy of Sciences of the USSR 31 (1941) 99–101.

[35] E. Novikov, D. Dommermuth, Distribution of droplets in a turbulent spray, Physical Review E 56 (1997) 5479-5482. https://journals.aps.org/pre/abstract/10.1103/PhysRevE.56.5479.

[36] M. Gorokhovski, V. Saveliev, Analyses of kolmogorov's model of breakup and its application into lagrangian computation of liquid sprays under airblast atomization, Physics of Fluids 15 (2003) 184–192. https://doi.org/10.1063/1.1527914.

[37] N. Rimbert, 2010. Simple model for turbulence intermittencies based on self-avoiding random vortex stretching. Physical Review E. 81, 056315. https://doi.org/10.1103/PhysRevE.81.056315.

[38] E. Urionabarrenetxea, A. Avello, A. Rivas, J.M. Martín, 2021. Experimental study of the influence of operational and geometric variables on the powders produced by close-coupled gas atomization. Materials & Design. 199, 109441. https://doi.org/10.1016/j.matdes.2020.109441.

[39] J. Wang, M. Xia, J. Wu, C. Ge, Nozzle clogging in vacuum induction melting gas atomization: influence of the delivery tube and nozzle coupling, Arch. Metall. Mater. 67 (2022) 1359-1370. https://doi.org/10.24425/amm.2022.141063.